Rational development of Nile red derivatives with significantly improved specificity and photostability for advanced fluorescence imaging of lipid droplets

Huanlong Zheng [a,1], Hao Sha [b,c,1] , Ri Zhou [a,1], Yu Wu [c], Chenguang Wang [a,*] , Shangguo Hou [c,**], Geyu Lu [a,***]

[a] *State Key Laboratory of Integrated Optoelectronics (JLU Region), Key Laboratory of Advanced Gas Sensors of Jilin Province, College of Electronic Science & Engineering, Jilin University, Changchun, 130012, China*
[b] *School of Computer Science and Technology, Harbin Institute of Technology (Shenzhen), Shenzhen, 518006, China*
[c] *Institute of Systems and Physical Biology, Shenzhen Bay Laboratory, Shenzhen, 518132, China*

ARTICLE INFO

ABSTRACT

Since the first report of Nile Red as a fluorescent probe for lipid droplets (LDs) imaging was published in 1985, this fluorescent probe has been widely used for nearly 40 years, and so far, it is still one of the most commonly used probes for LDs imaging. Although Nile Red has achieved continuous success, it has gradually emerged two major limitations (poor LDs specificity and low photostability) which directly limit the study of LDs via advanced fluorescence imaging techniques. In this context, we have developed a new synthetic route to conveniently prepare a series of Nile Red derivatives (NR-1 to NR-15). With these 15 derivatives in hand, the relationships between molecular structures and their properties (LDs specificity, photostability) have been comprehensively investigated. Consequently, we have rationally designed a new Nile Red derivative, NR-11, which exhibits significantly improved LDs specificity and photostability. Utilizing this new LDs probe, we have successfully conducted various advanced fluorescence imaging, *e.g.* time-lapse three-dimensional (3D) confocal imaging of cells, time-lapse 3D dynamic tracking of a single LD, and two-photon 3D imaging of tissues. These advanced imaging results not only demonstrate the utility of this new fluorescent probe but also provide novel insights into the cell biology study of LDs.

1. Introduction

Lipid droplets (LDs) are ubiquitous organelles found in almost all eukaryotic cells, consisting of neutral lipid cores and surrounding phospholipid monolayer membranes. For a long time, LDs were thought to be inert fat particles that stored excess lipids in cells. However, more recent studies have continuously discovered that LDs play critical roles in a variety of cellular processes such as energy balance, lipid metabolism, membrane protein production, membrane trafficking, and so on (Mathiowetz and Olzmann, 2024; Olzmann and Carvalho, 2019). Furthermore, numerous metabolic disorders, such as diabetes, coronary artery disease, cardiomyopathy, and fatty liver, have been recently proven to be closely related to an abnormal increase in the size and number of LDs (Shen et al., 2024; Zadoorian et al., 2023). As a result, the study of LDs has emerged as one of the most appealing subjects in the field of cell biology in recent years.

To visualize LDs and figure out their versatile functions, fluorescence imaging techniques have been widely employed owing to their high spatial resolution, real-time, and non-invasive features. Consequently, a variety of lipophilic fluorescent probes have been reported for LDs fluorescence imaging, *e.g.* Nile Red (Cao et al., 2025; Greenspan and Fowler, 1985), BODIPY 493/503 (Cao et al., 2025), solvatochromic probe AP-C12 (Kajiwara et al., 2022), HClO-reactive probe LDM (Kong et al., 2024), AIEgen-type 1,8-naphthalimide derivative and TPAPhCN

(Henwood et al., 2024; Wang et al., 2021c), photoconvertible probe SC-P (Saladin et al., 2023), fluorogenic probe LD-FG (Chen et al. 2021, 2024), ESIPT-type probe PPC (Guo et al., 2021), and so on (Collot et al., 2018; Dai et al., 2023; Hong et al., 2023; Liu et al. 2023, 2025; Wang et al. 2021b, 2023, 2024, 2025; Wu et al., 2024; Xiong et al., 2024). Since the first report on Nile Red labeled LDs fluorescence imaging was published in 1985 (Greenspan and Fowler, 1985), this classical probe has been widely used for up to 40 years, and so far, it is still the most commonly used one for LDs imaging (Cao et al., 2025). Although Nile Red has achieved continuous success over many years, it has two shortcomings: 1) the LDs specificity is not high and Nile Red would stain LDs as well as other organelles/areas in cells; 2) the photostability is relatively low, and this would cause serious photobleaching during time-lapse imaging (Scheme 1A). With the rapid progress of fluorescence imaging techniques, these two shortages of Nile Red have become even more severe. Undoubtedly, there is an urgent requirement to overcome these two shortages. However, directly limited by the synthetic route and further functionalization strategy, the synthesis of various Nile Red derivatives is very complicated and time-consuming (Danylchuk et al., 2021; Hornum et al., 2020; Madea et al., 2020; Martinez and Henary, 2016). Consequently, the shortcomings of LDs specificity and photostability of Nile Red have rarely been concerned and have remained as bottlenecks for a long period.

In this context, we herein have developed a new synthetic route to conveniently prepare a family of Nile Red derivatives NR-1 to NR-15 (Scheme 1B–D). With these 15 derivatives in hand, we have comprehensively investigated the relationship between molecular structures and LDs specificity as well as the relationship between molecule structures and photostability. Consequently, we have rationally developed a new Nile Red derivative NR-11 with significantly improved LDs specificity and photostability. Moreover, utilizing this new LDs probe NR-11, we have successfully conducted a series of advanced fluorescence imaging: *e.g.* time-lapse three-dimensional (3D) confocal imaging of LDs in cells, time-lapse 3D dynamic tracking of even a single LD, and two-photon 3D imaging of LDs in tissues. These advanced imaging results not only demonstrate the utility of this newly developed fluorescent probe NR-11 but also provide novel insights into the cell biology study of LDs.
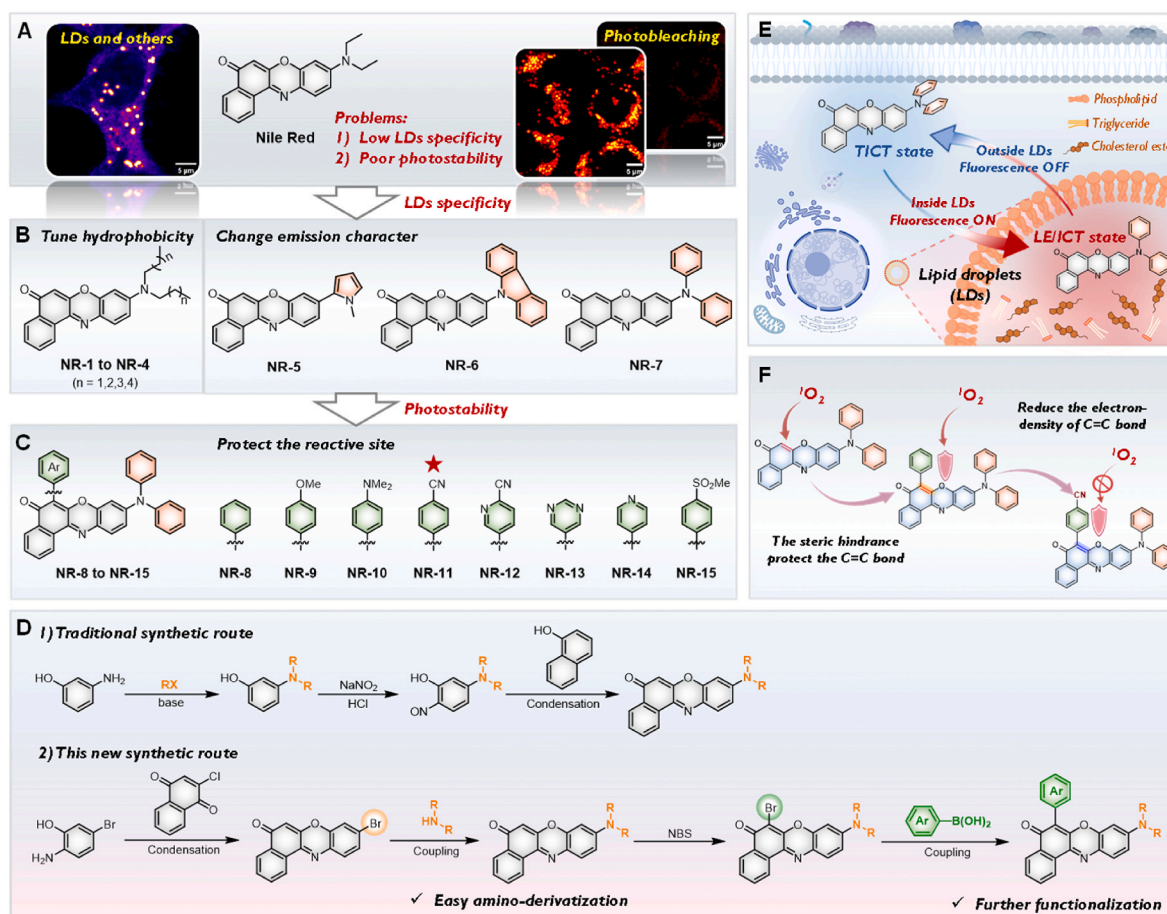
2. Material and methods

2.1. Synthesis and characterization

The synthetic details, structural characterization data (^{1}H NMR, ^{13}C NMR and single crystal structure), spectral measurements, theoretical calculation methods and general fluorescence imaging experiments have been described in the Supplementary material.

2.2. Time-lapse 3D confocal imaging of cells

The imaging experiments were conducted with *xyzt* shooting mode under Leica TCS SP8 imaging system with following set: λ_{ex} = 530 nm, λ_{em} = 540–780 nm, a scan speed of 100 Hz, a pixel resolution of 72.2 nm × 72.2 nm, a *z*-step of 300 nm, a total of 15 sets of 3D imaging. In

Scheme 1. (A) The problems of Nile Red as the most commonly used LDs fluorescent probe for 40 years. (B, C) The molecular design strategies to improve the LDs specificity and the photostability. (D) The traditional synthetic route of Nile Red derivatives and this new synthetic route. (E) The TICT-type molecule NR-11 displaying the highly emissive LE/ICT state in LDs while the non-emissive TICT state in cytoplasm, and thus low fluorescence background in cytoplasm for imaging. (F) The improvement of photostability via protecting the reactive C=C bond nearby the C=O group.

addition, a microscopy-suited incubator was employed to control the temperature (37 °C) and CO_2 concentration (5 %).

2.3. Time-lapse 3D dynamic tracking of single LD

For the tracking of intracellular single LD, we have developed a single-particle tracking system capable of real-time tracking at millisecond-nanometer scale. Briefly, Electro-Optic Deflector (EOD) and Tunable Acoustic Gradient (TAG) lens enable rapid 3D scanning within the target focal area. The 3D coordinate of target particle in the scanning volume is calculated in real time. Then feedback is applied to the piezo stages to compensate the motion of particle. During tracking, the 561 nm laser (LCX-561L-50-CSB-PPA, OXXIUS) power was set to 20 mW, and a ND filter (Lbtex, NDFA10-20, OD2) was used to regulate the power. The objective lens in this system was $100\times$ oil-immersion objective lens (Leica, HC PL APO $100\times/1,40$ OIL CS2, NA 1.5), and an emission filter (FF01-630/38-25, Semrock) was employed. To induce ferroptosis, the HeLa cells labeled with NR-11 were treated with erastin (10 μM) for 15 min.

3. Results and discussion

3.1. Molecular design and synthesis

To significantly improve the LDs specificity, we have implemented two strategies (Scheme 1B). One strategy is to tune the hydrophobicity of molecules, and accordingly NR-1 to NR-4 with different alkyl chains have been synthesized. Considering the hydrophobic nature of LDs, NR-1 to NR-4 indeed exhibit higher LDs specificity than Nile Red. However, the effectiveness of this strategy is moderate; the improvement of LDs specificity of NR-1 to NR-4 in terms of the signal-to-noise ratio is only about 2 times that of Nile Red in fluorescence imaging (*vide infra*).

Another strategy to improve the LDs specificity is to tune the emission character of molecules. The newly synthesized molecules NR-5 to NR-7 with the twisted intramolecular charge transfer (TICT) character are anticipated to display intense fluorescence in LDs (low polarity environment) but faint emission in cellular cytoplasm (high polarity) (Scheme 1E). In contrast, Nile Red with the intramolecular charge transfer (ICT) character would exhibit strong emission in both LDs and cytoplasm. Consequently, it is believed that the TICT-type molecules NR-5 to NR-7 would display much lower background in fluorescence imaging and thus dramatically higher LDs specificity than the ICT-type molecule Nile Red. Indeed, the LDs specificity of NR-7 is up to 8 times that of Nile Red in fluorescence imaging (*vide infra*), highlighting the effectiveness of TICT strategy in LDs specificity.

Because TICT-type NR-7 displays the highest LDs specificity among these derivatives, we have thereafter focused on this fluorophore to further improve the photostability (Scheme 1C). In the ^{1}H NMR spectrum of NR-7, it is found that the chemical shift of the proton of the C=C bond nearby the C=O group is much smaller than the other protons (Fig. S1). We therefore speculated that this C=C bond may be the reactive site under the photo-irradiation (*i.e.* photobleaching) (Scheme 1F). Consequently, NR-8 to NR-15 with various substituents have been synthesized to protect that reactive site, and indeed these derivatives exhibit much higher photostability than NR-7 (*vide infra*). Among these derivatives, NR-11 displays the highest performance in terms of LDs specificity and photostability, and thus has been applied in various advanced fluorescence imaging.

For the synthesis of Nile Red derivatives, we herein developed a new synthetic route (Scheme 1D). The first step is a condensation between 2-amino-5-bromophenol and 2-chloro-1,4-naphthoquinone under base conditions (Fig. S2) (Agarwal and Schaefer, 1980). The thus produced bromide intermediate would readily undergo the Buchwald-Hartwig/Suzuki-Miyaura coupling with various amines/boric acid esters to generate NR-1 to NR-7 (Fig. S3). Next, NR-7 was smoothly mono-brominated by NBS and the bromide product would subsequently

react with various organoboronic acids via Suzuki-Miyaura coupling to yield NR-8 to NR-15 (Fig. S4). The molecular structures of NR-1 to NR-15 were fully characterized by ^{1}H NMR and ^{13}C NMR spectra, and the target fluorescent probe NR-11 has been further confirmed by X-ray single-crystal analysis (Fig. S5).

Notably, in comparison to the traditional synthetic route of Nile Red derivatives (Scheme 1D) (Danylchuk et al., 2021; Hornum et al., 2020; Madea et al., 2020; Martinez and Henary, 2016), our new synthetic route has the distinguished advantage of easy derivatization/functionalization. This advantage lies in the fact that our new synthetic route provides two very useful bromide intermediates which can readily undergo the Buchwald-Hartwig/Suzuki-Miyaura coupling reactions. As a result, up to 15 Nile Red derivatives (NR-1 to NR-15) could be conveniently synthesized. Moreover, the two bromide intermediates enable to easily introduce various substituents to tune the hydrophobicity or the water-solubility for the other applications.

3.2. Photophysical properties

The photophysical properties of Nile Red and NR-1 to NR-7 have been examined in organic solvents with various polarities. Overall, Nile Red and NR-1 to NR-4 display moderate emission solvatochromism: their emission maxima (λ_{em}) are only slightly red-shifted from ~570 nm in toluene to ~615 nm in acetone, and the fluorescence quantum yields (Φ_F) are maintained quite high (78 %–96 %) regardless of the solvent polarity (Fig. 1A, Fig. S6, and Table S1). In sharp contrast, NR-5 to NR-7 exhibit significant emission solvatochromism: *e.g.* the λ_{em} of NR-7 is largely red-shifted from 599 nm in toluene to 692 nm in acetone, and the Φ_F is dramatically quenched from 99 % to 0.2 % (Fig. 1B, Fig. S7, and Table S2). In addition, the fluorescence of NR-7 is insensitive to the pH values (Fig. S8). The different solvatochromism behaviors reveal that Nile Red and NR-1 to NR-4 should display ICT character in the excited state while NR-5 to NR-7 exhibit TICT character (Hanaoka et al., 2022; Wang et al. 2020, 2021a; Zhang et al., 2024).

To gain a deep insight into the photophysical properties, we have comprehensively performed theoretical calculations. First, the energy orbitals have been calculated: the HOMO and LUMO of Nile Red are overlapped with each other, while those of NR-5 to NR-7 are significantly separated (Fig. S9). The HOMO of NR-5 to NR-7 is mainly composed of the electron-donating amino group, and the LUMO is primarily located at the electron-accepting phenoxazone moiety. The large separation between HOMO and LUMO reveals a potential dramatic change of molecule conformation upon photon excitation. Second, the molecule conformations have been calculated in both ground state (S0) and excited state (S1). It is found that the twist angle (θ) between the amino group and the phenoxazone moiety is negligible in both S0 ($\theta = 5.4°$) and S1 ($\theta = 5.8°$) for Nile Red (Fig. 1A), while that angle would be largely increased from 28.9° in S0 to 88.7° in S1 for NR-7 (Fig. 1B). As a result, the separation between HOMO and LUMO of NR-7 is even more pronounced in S1 than that in S0 (Fig. S10). Third, the twist angle dependent S1 energy has been calculated. As shown in Fig. 1C, upon increasing the twist angle, the S1 energy of Nile Red would be gradually improved and then meet a large energy barrier up to 1.7 eV. In contrast, there is no such energy barrier for NR-7 and its S1 energy would be largely decreased upon twisting for 90°. These calculations demonstrate that the electron-donating -NPh$_2$ group, which largely contributes to the HOMO of NR-7 and thus results in a significant separation between HOMO and LUMO, tends to twist 90° in S1. In sharp contrast, the -NEt$_2$ group of Nile Red would maintain a non-twisted conformation in S1. This result well explains the TICT character of NR-7 and the ICT character of Nile Red in theory (Fig. 1D).

To experimentally prove the TICT character, as a long-term challenge in the field of fluorescence molecules, we have measured the temperature-dependent fluorescence spectra of Nile Red and NR-7 in THF solutions. As shown in Fig. 1E, upon increasing the temperature from 118 K to 218 K (THF melting point: 165 K), the fluorescence
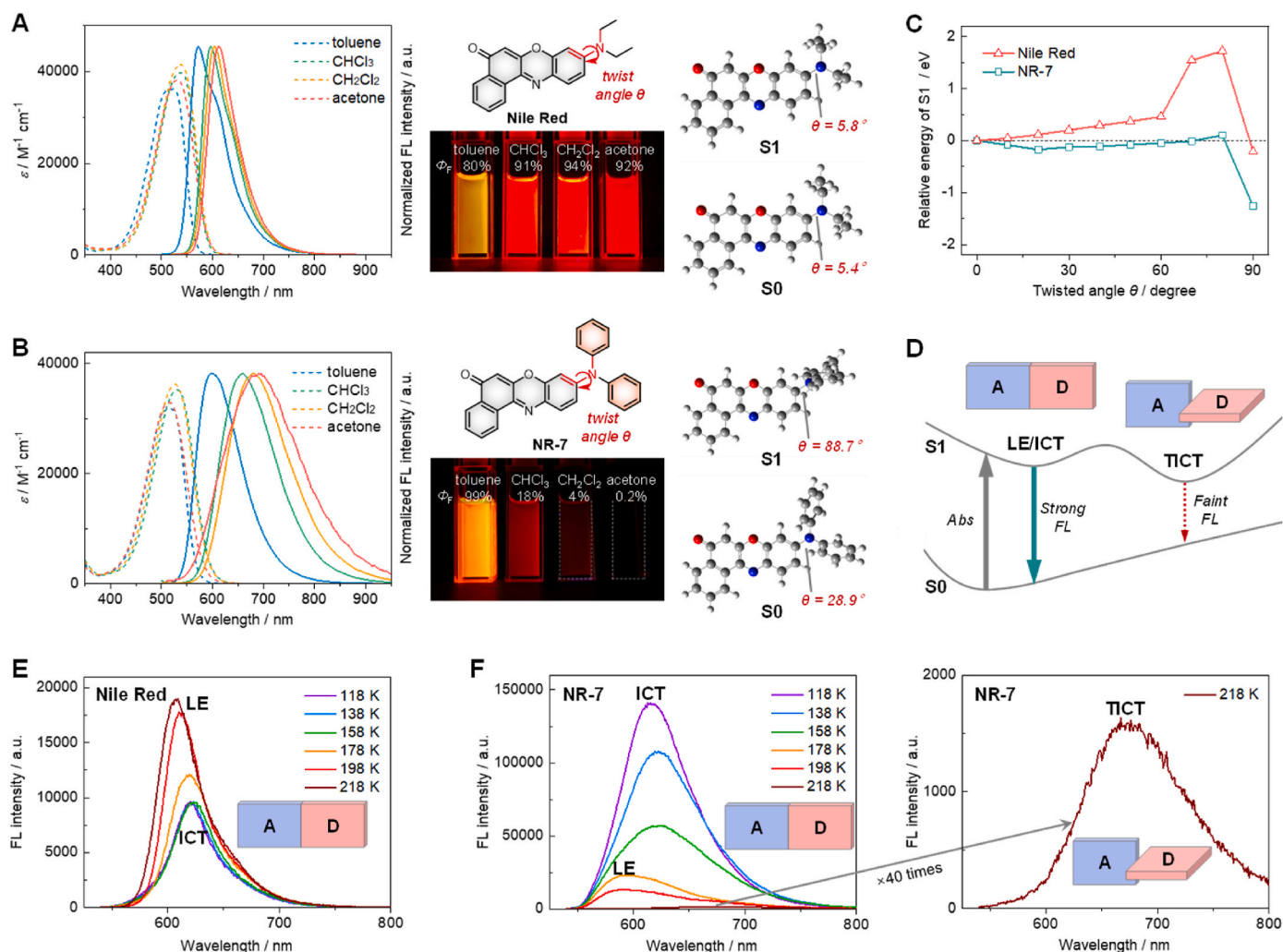
Fig. 1. (A, B) Photophysical spectra in various solvents, photographs under UV light, and optimized molecule conformations (B3LYP/6-31G*) in ground state S0 and in excited state S1 of Nile Red and NR-7. (C) The twist angle dependent S1 energies of Nile Red and NR-7 at the M06-2X/def2-SVP level in water using cLR solvent formalism. (D) The schematic diagram of D-A type molecule exhibiting strong LE/ICT emission or faint TICT emission. (E, F) Temperature-dependent (118–218 K) fluorescence spectra of Nile Red and NR-7 in THF solutions (10^{-6} M).

intensity and wavelength of Nile Red do not change substantially. In contrast, the fluorescence intensity of NR-7 is dramatically decreased by up to 90 times from 118 K to 218 K, and the fluorescence wavelength is also largely red-shifted (Fig. 1F). Moreover, in terms of the fluorescence spectrum shape of NR-7, the emission band located at 615 nm gradually disappears, and the emission band at 590 nm gradually emerges from 118 K to 178 K. Particularly, an intermediate state of this change is observed at 158 K: both the 615 nm band and the 590 nm band could be distinguished. From 178 K to 218 K, a similar change in the fluorescence spectrum is observed: the 590 nm band disappears, the 675 nm band emerges, and an intermediate state containing both bands is found at 198 K (Fig. S11). These temperature-dependent fluorescence spectra directly prove that there are three kinds of excitation states for NR-7. Further considering the fluorescence wavelength and intensity, the three emission bands are assigned as follows: 590 nm for local excitation (LE) state, 615 nm for ICT state, and 675 nm for TICT state. Thus, we have successfully confirmed the red-shifted and non-emissive TICT state of NR-7, and especially have directly distinguished the TICT state from the ICT state.

We next performed femtosecond time-resolved absorbance (fs-TA) measurements to study the excited-state dynamics of Nile Red and NR-7 (Fig. S12–S13). In non-polar cyclohexane and low-polar toluene, the fs-TA spectra of Nile Red are dominated by two distinct negative bands of

~530 nm and ~620 nm, which are attributed to the stimulated emission (SE) of LE state and the SE of ICT state, respectively (Fig. S12A–B). In high-polar acetone, the negative band of ~615 nm corresponds to the SE of ICT state (Fig. S12C). The assignments of LE and ICT states have been further confirmed by the global analysis of fs-TA spectra. In a similar manner, the fs-TA spectra of NR-7 have also been analyzed: LE state in cyclohexane, LE and ICT state in toluene, and TICT state in acetone (Fig. S13A–C). Due to the effect of excited state absorption (ESA), the wavelength of observed SE band of TICT state (~750 nm) in acetone is substantially longer than that of the TICT fluorescence (~690 nm). Based on the fs-TA results, the excited state dynamics of Nile Red and NR-7 have been comprehensively analyzed. Upon increasing the polarity from cyclohexane to acetone, the decay process of Nile Red is changed from LE state to ICT state (Fig. S12D–F), while that of NR-7 is transferred from LE state to ICT state and until TICT state (Fig. S13D–F). Moreover, the decay process from TICT state (37 ps for NR-7) is much faster than that of LE (2.9 ns for Nile Red, 3.1 ns for NR-7) and ICT state (4.1–5.4 ns for Nile Red, 4.3 ns for NR-7). The very fast TICT decay is consistent with the timescale of nonradiative process, and thus results in a nearly non-emissive behavior of NR-7 in acetone ($\Phi_F = 0.2$ %). In contrast, LE/ICT decay (2.9–5.4 ns) is in the fluorescence timescale, and therefore the intense fluorescence is observed for Nile Red in cyclohexane, toluene and acetone as well as NR-7 in cyclohexane and toluene

(Φ_F = 53 %–99 %). In short, through the fs-TA study, we have experimentally captured the LE, ICT, and TICT states, and have revealed that the TICT decay is an ultra-fast nonradiative process (~10^1 ps) and the LE/ICT decay is a relatively slow fluorescence process (~10^3 ps).

Based on the TICT-type fluorophore NR-7, we thereafter introduced various substituents at the ortho-position of C=O to result in the derivatives NR-8 to NR-15. The photophysical properties of these derivatives have also been evaluated (Fig. S14–S16, Table S3). Overall, NR-8 and NR-10 to NR-15 display strong solvatochromism similar to the parent molecule NR-7: e.g. the λ_{em} of NR-11 is largely red-shifted from 618 nm in toluene to 703 nm in acetone and the Φ_F is dramatically quenched from 82 % to 0.2 %. This is reasonable when comparing their HOMO/LUMO characters (Fig. S17–S18). Among these derivatives, NR-9 and NR-10 exhibit weak emission or non-emission. This is because the introduction of electron-donating moiety -OMe or -NMe$_2$ significantly changes the HOMO distribution.

3.3. Photostability

The photostability of Nile Red derivatives has been evaluated in 1,4-dioxane solutions under the irradiation of 530 nm LED. As shown in Fig. 2A, the absorption intensities of NR-7 are quickly decreased upon irradiation, revealing the fast photobleaching process and low photostability. Introducing a -Ph substituent to NR-7 has enabled the resulting derivative NR-8 to display significantly better photostability (Fig. 2B). Further installing a strong electron-withdrawing -CN group to NR-8 has endowed NR-11 with even higher performance (Fig. 2C). After irradiation for 80 min, almost no photobleaching has been observed for NR-11, highlighting its outstanding photostability. The successive improvement

of photostability from NR-7 to NR-8 and until NR-11 has experimentally demonstrated that, as speculated by the NMR study (vide ante, Fig. S1), the C=C bond nearby the C=O group is indeed the reactive site under the photo-irradiation. The photostability of other Nile Red derivatives has also been evaluated (Fig. S19–S20). Overall, NR-12 to NR-15 display outstanding photostability similar to NR-11, while NR-5 and NR-6 exhibit even lower photostability than NR-7 and Nile Red (Fig. 2D). The photostability of NR-7 has been also evaluated in the various solvents (Fig. S21). It is found that the solvent has dramatic effect on the photostability. However, the reason is unclear in current stage. In addition, the pH effect has been studied and no obvious difference on the photostability of NR-7 (Fig. S22).

A well-known photobleaching mechanism of fluorescent molecules is that the singlet oxygen ($^1O_2$) generated by the fluorescent molecules under photo-excitation would oxidize the fluorescent molecule itself (Baral and Thomas III, 2015; Kaur et al., 2008; Shank et al., 2013; Shank et al., 2009; Wan et al., 2024). We have therefore studied the $^1O_2$ effect. Chlorin e6 (Ce6), a widely used photosensitizer, was employed to efficiently generate $^1O_2$ under 405 nm LED irradiation. As shown in Fig. S23, NR-7 itself was rather stable under 405 nm irradiation. However, upon mixing with Ce6 (molar ratio of 1:1), NR-7 would be quickly photobleached under the identical irradiation conditions. This result directly proves that the $^1O_2$ oxidation is an important factor for NR-7 photobleaching.

Based on these experiments, we have proposed a possible photobleaching mechanism for Nile Red derivatives. That is oxidation of the C=C bond nearby the C=O group by $^1O_2$ (Scheme 1F). Moreover, the fact that NR-8 and NR-11 display higher resistance to the $^1O_2$ oxidation than NR-7 also confirms this photobleaching mechanism (Fig. S23). This
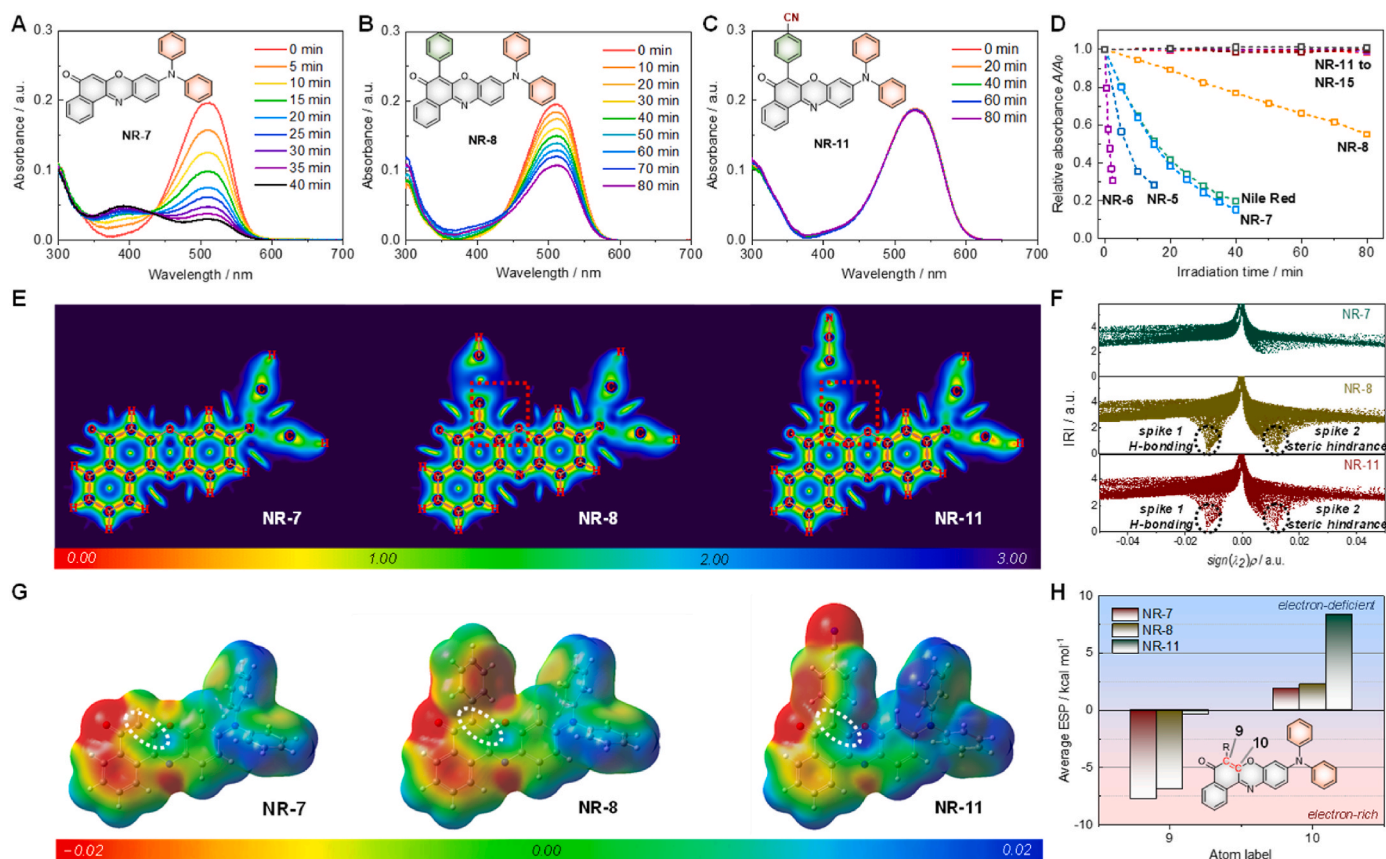

Fig. 2. (A–C) Absorption spectra of NR-7, NR-8, and NR-11 in 1,4-dioxane solutions under the irradiation of 530 nm LED (~650 mW/cm^2) for different time. (D) Relative absorbance values of Nile Red derivatives as a function of irradiation time. (E) The color-filled IRI maps of NR-7, NR-8, and NR-11. The scales of color bars are given in a.u. (F) The scatterplot calculations between IRI and $sign(\lambda_2)\rho$ of the square-marked regions on the IRI maps. (G) The ESP distributions of NR-7, NR-8, and NR-11. The scales of color bars are given in hartree. (H) The average ESP values of carbon-9 and carbon-10 (C=C bond) of NR-7, NR-8, and NR-11.

is because the introduction of a -Ph substituent would provide a bulky steric hindrance from the attack of $^1O_2$ for NR-8, and further installation of the strong electron-withdrawing -CN group would decrease the electron density of the C=C bond (*i.e.* decrease the reactivity to $^1O_2$) for NR-11.

To deeply understand the steric effect of -Ph substituent and the electron-withdrawing influence of -CN group on improving the photo-stability of Nile Red derivatives, we have performed the theoretical calculations of interaction region indicator (IRI) and electrostatic potential (ESP). The IRI is a recently developed real-space function that can directly reveal the weak interactions and chemical bonds for molecules (Gao et al., 2023; Lu and Chen, 2012, 2021). As shown in Fig. 2E, the color-filled maps of IRI demonstrate that in comparison to NR-7, there are additional discernible distributions of IRI functions (marked by squares) between the -Ph substituents and the phenoxazone moieties for NR-8 and NR-11. This result suggests the existence of considerable weak interactions. To further analyze these weak interactions, the scatterplot calculations between IRI and $sign(\lambda_2)\rho$ have been performed (Fig. 2F) and the corresponding isosurface maps of IRI have been produced (Fig. S24). These calculations reveal that the additional IRI distributions of NR-8 and NR-11 are contributed by the hydrogen bonding (spike 1, green color pattern) and the steric hindrance (spike 2, red color pattern). Because the hydrogen bonding is an attractive interaction, the repulsive

steric hindrance (balanced with the hydrogen bonding) would be rather strong and stable, and hence could effectively protect the reactive C=C bond from the attack of $^1O_2$. As a result, it is reasonable to observe that NR-8 and NR-11 display significantly higher photostability than NR-7.

Next, the ESP calculations were conducted to explain why NR-11 is more photostable than NR-8. As shown in Fig. 2G, the electron density of reactive C=C bond of NR-11 is obviously lower than that of NR-7 and NR-8, demonstrating the significant electron-withdrawing effect of -CN group. The average ESP values of carbon-9 and carbon-10 (C=C bond) of NR-11 are -0.37 kcal mol^{-1} and 8.34 kcal mol^{-1}, respectively, which are much more positive than those of NR-7 (-7.78 kcal mol^{-1} and 1.89 kcal mol^{-1}) and NR-8 (-6.91 kcal mol^{-1} and 2.27 kcal mol^{-1}) (Fig. 2H). Therefore, the C=C bond of NR-11 should be significantly less reactive toward the electrophilic $^1O_2$ than that of NR-7 and NR-8. Accordingly, a much higher photostability would be expected for NR-11.

3.4. Fluorescence imaging property

First, we have studied the LDs labelling specificity of these Nile Red derivatives. NR-5 to NR-6 and NR-9 to NR-10 were not included because of their low photostability and the weak fluorescence, respectively. As shown in Fig. 3A, the HeLa cells stained with Nile Red (2 μM, 2 h) display strong fluorescence background in cellular cytoplasm. The
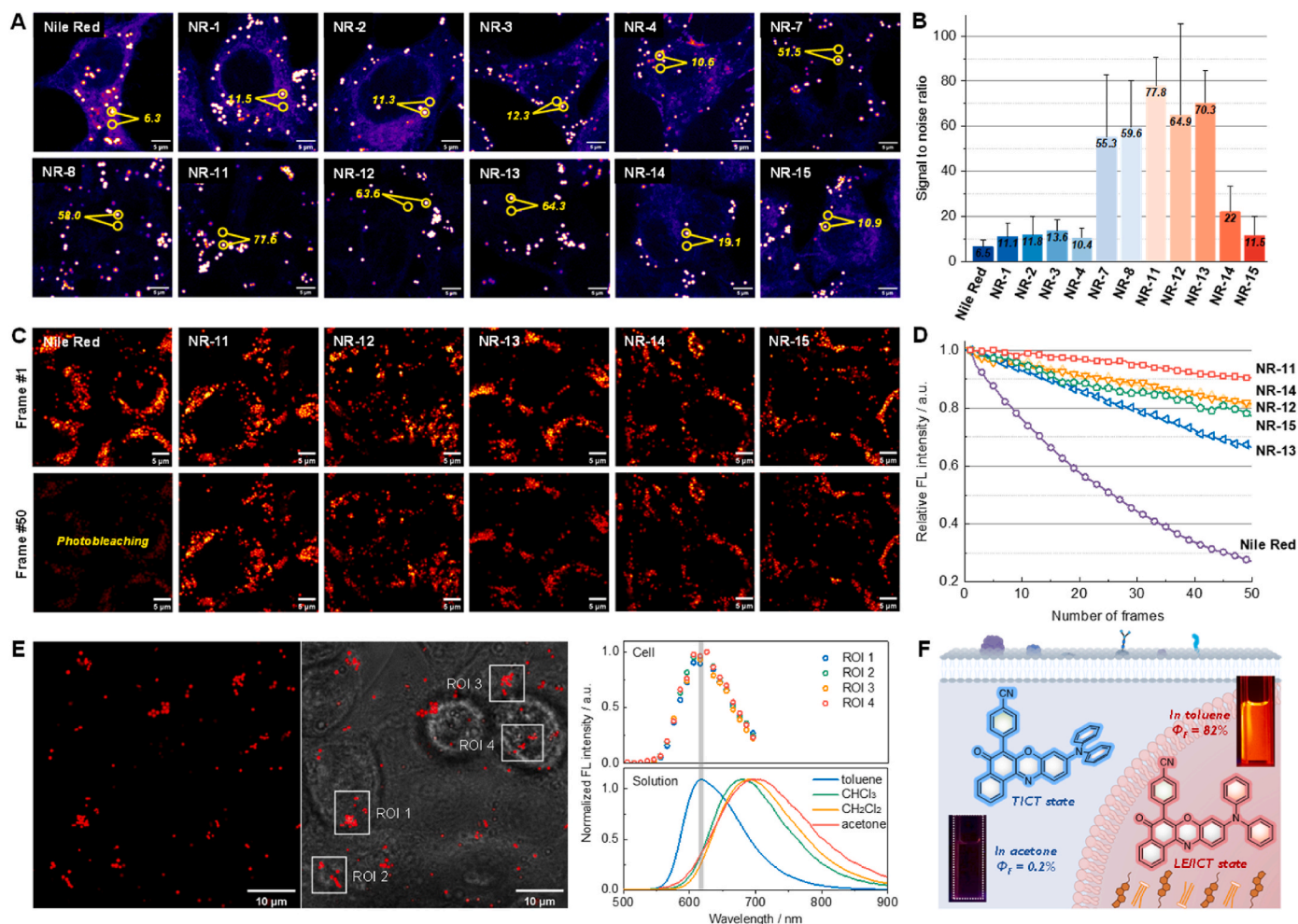

Fig. 3. (A, B) Comparison of the LDs labeling specificity of Nile Red derivatives: the confocal images of HeLa cells stained with various probes (2 μM, 2 h) and their statistical study of signal-to-noise ratio ($n = 40$). Scale bar: 5 μm. (C, D) Comparison of the photostability of Nile Red derivatives under harsh excitation conditions (about 100 times the normal imaging laser power, 488 nm): frame #1 and frame #50 of continuous confocal images, and the relative fluorescence intensity of confocal images plotted as a function of the image frame number. Scale bar: 5 μm. (E) The in-situ spectrum scanning fluorescence imaging of NR-11 in living HeLa cells: the fluorescence and bright field images, the fluorescence spectra in cells and in solutions. Scale bar: 10 μm. (F) The highly emissive LE/ICT state of NR-11 in toluene or in LDs and the non-emissive TICT state in acetone or in cytoplasm.

signal-to-noise ratio (S/N ratio, the ratio of fluorescence intensities between LDs and their nearby cytoplasm areas), which is employed to quantitatively evaluate the LDs specificity of fluorescent probe, is determined to be 6.5 ± 3.1 ($n = 40$) for Nile Red (Fig. 3B). This performance is quite insufficient for LDs fluorescence imaging, especially for the newly-developed advanced imaging methods. Upon increasing the hydrophobicity of fluorescent probes by employing longer alkyl chains, NR-1 to NR-4 exhibit lower fluorescence background in cytoplasm (*i.e.* higher LDs specificity) than Nile Red. Accordingly, the S/N ratios of NR-1 to NR-4 are improved to the range of 10.4 ± 4.5 to 13.6 ± 5.0 (about two times that of Nile Red). Furthermore, tuning the ICT emission character (Nile Red and NR-1 to NR-4) to the TICT emission character (NR-7 to NR-8 and NR-11 to NR-13) has endowed the TICT-type fluorescence probes with even higher LDs specificity. For instance, the S/N ratio of NR-11 is as high as 77.8 ± 12.9 ($n = 40$), which is about 12 times that of Nile Red. In addition, two TICT-type fluorescence probes, NR-14 (the S/N ratio of 22.0 ± 11.4, $n = 40$) and NR-15 (the S/N ratio of 11.5 ± 8.5, $n = 40$) display significantly lower LDs specificity than the other TICT-type ones (the S/N ratios of 55.3 ± 27.3 to 77.8 ± 12.9, $n = 40$). This is probably because the pyridine and sulfone groups with high electron density (ESP values) may form strong intermolecular interactions with the proteins in cytoplasm (Fig. S25).

Based on the comprehensive study, we have obtained three ideas for rational development of new fluorescent probes with high LDs specificity. First, the TICT-type fluorescent probes would display much higher LDs specificity than the ICT-type ones, because the TICT-type probes quench their fluorescence in cytoplasm (high polarity environment) while the ICT-type ones would not (Scheme 1E). Second, the hydrophobicity of fluorescent probe also influences the LDs specificity, but the effectiveness is weaker than the change of emission character from ICT to TICT. Third, besides of the emission character and the hydrophobicity, the substituent group (*e.g.* pyridine and sulfone) may also affect the LDs specificity.

Next, the photostability of NR-11 to NR-15 (which are very photostable in solution) was evaluated in cells. As shown in Fig. 3C, after continuously recording 50 confocal images under harsh excitation conditions (about 100 times the normal imaging laser power, 488 nm), Nile Red is seriously photobleached and the fluorescence signal is only left 27 % of its initial values (Fig. 3D). In contrast, NR-11 to NR-15 are very photostable, and particularly NR-11 maintains the highest performance (91 %) after recording 50 confocal images under the strong laser excitation. To quantitatively evaluate the photostability of Nile Red derivatives, their photobleaching decay curves were fitted with a single exponential function (Fig. S26). Based on the comparison of photobleaching kinetics, it is observed that the photostability of NR-11 is 7.9 times that of Nile Red.

In short, NR-11 is the best choice among these Nile Red derivatives in terms of the high LDs specificity and superior photostability. Moreover, the LDs specificity and photostability of NR-11 are also significantly higher than those of another representative LDs probe BODIPY 493/503 (Fig. S27−S28). The colocalization experiments demonstrate that NR-11 could be used in various cell lines (HeLa, HepG2 and 4T1) for LDs imaging (Fig. S29) and does not stain other cellular organelles (such as mitochondria and lysosomes) (Fig. S30). We have therefore further measured the fluorescence spectrum of NR-11 in LDs of living HeLa cells by in-situ spectrum scanning fluorescence imaging. As shown in Fig. 3E, the λ_{em} of NR-11 is about 615 nm in LDs, which is very close to the value (618 nm) in toluene solution. This result reveals that the polarity of LDs is comparable to that of toluene, and thus the TICT-type probe NR-11 would be highly emissive in LDs (Fig. 3F). In addition, the cytotoxicity of NR-11 has also been assessed. As demonstrated by the 3-(4,5-dimethylthiazol-2-yl)-2,5-diphenyltetrazolium bromide (MTT) test, the fluorescent probe does not affect the cell viability within 24 h even at a high concentration of 10 μM (Fig. S31). All of these results demonstrate that NR-11 should be an excellent LDs fluorescence probe in place of Nile Red, a classical LDs probe widely used from 1985 to the present day.

3.5. Time-lapse 3D confocal imaging of cells

Integrating the temporal dimension (*i.e.* time-lapse) into 3D confocal imaging, also known as 4D confocal imaging, allows for real-time visualization of the cellular organelles in a 3D space and further precise monitoring of their changes in number and size. Undoubtedly, the time-lapse 3D confocal imaging is a very powerful tool for biological study. However, this advanced imaging method has two strict requirements for the fluorescent probe. One requirement is the high labeling specificity of probe, which is crucial for clearly visualizing the 3D spatial distribution of organelles (Fig. S32). Another requirement is the high photostability of probe, because several hundred confocal frames are generally recorded for this advanced imaging. Taking into consideration the distinctive features of NR-11, we have employed this probe for time-lapse 3D confocal imaging to monitor the change of LDs during starvation (an important energy metabolism process closely associated with LDs).

For this experiment, the HeLa cells stained with NR-11 were kept in Hank's balanced salt solution (HBSS) for starvation and imaging. At a z-depth of 11.4 μm, a total of 39 confocal frames were recorded and further reconstructed to produce one 3D image (Fig. 4A). With an interval of 20 min, fifteen 3D images were repeatedly acquired in 280 min (Fig. S33). Therefore, up to 585 confocal frames were scanned at the same area of cells for this time-lapse 3D confocal imaging. Notably, almost no photobleaching was observed during the imaging process. In the time-lapse 3D confocal imaging, it has been found that: 1) the distribution of LDs is gradually changed from discrete to aggregate upon starvation (Fig. 4A); 2) the number of LDs is significantly decreased (Fig. 4B); 3) the size of LDs is maintained consistently (Fig. 4B, Fig. S34). Based on these observations, it is proposed that the LDs would be consumed one by one to supply energy during starvation rather than all of the LDs metabolized at the same time via decreasing their sizes.

So far, there are three different pathways for the LDs mobilization proposed in the literature (Fig. 4C) (Laval and Ouimet, 2023; Rambold et al., 2015). The first pathway is macrolipophagy of LDs, which mainly involves the endocytosis of an entire LD within a lysosome to form an autolysosome and then the hydrolysis by lysosomal acid lipase (LAL) to release the free fatty acids (FAs). In this case, the number of LDs would be significantly decreased, while the size of LDs would remain constant. The second pathway is microlipophagy of LDs, which is similar to the macrolipophagy of LDs, with the only difference that a part of LD is endocytosed by a lysosome rather than an entire LD. In this process, the size of LDs would be obviously decreased, and the number of LDs may be unchanged. The third pathway is lipolytic metabolism of LDs, in which the LDs serve as transfer media of FAs between cytoplasm and mitochondria. In other words, the LDs would, on one hand, absorb the free FAs from cytoplasm to generate triglycerides (TAGs) and, on the other hand, hydrolyze the TAGs to result in FAs and then transfer FAs to mitochondria. In this pathway, the number of LDs would be stable, and the size of LDs may be changed or not. According to the imaging results, we can surely state that the macrolipophagy of LDs should be the major pathway for the starvation. Given the significant and contentious issue of whether starvation results in a decrease in the number of LDs (Bizjak Mali et al., 2013; Harvald et al., 2017; Nguyen and Olzmann, 2017; Rambold et al., 2015), our time-lapse 3D confocal imaging has undoubtedly answered this question and even revealed the metabolism mode of LDs during starvation.

3.6. Time-lapse 3D dynamic tracking of single LD

Benefiting from the superior photostability and specificity of NR-11, we have been able to track the dynamics of even single LD in 3D space. For this imaging experiment, an advanced 3D single-particle tracking system developed recently was employed (Hou et al., 2020). Two groups of LDs of HeLa cells, control group and erastin (a well-known ferroptosis inducer) stimulated group, were tracked to investigate the change of LDs
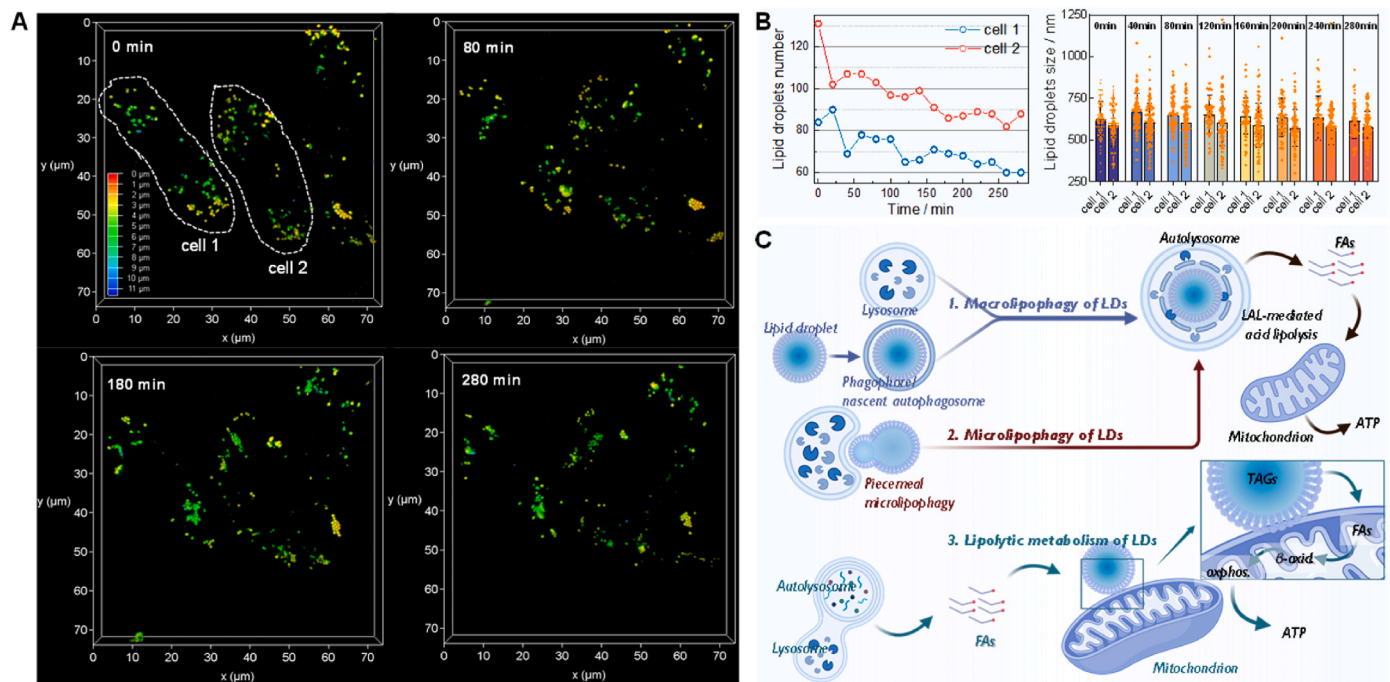
Fig. 4. (A) Time-lapse 3D confocal imaging of living HeLa cells stained with NR-11 under starvation stimulation. The 3D images (xyz: 74 × 74 × 11.4 μm³; top view) at different time spots (0 min, 80 min, 180 min, and 280 min) are shown. (B) The change of LDs number and the size distribution of LDs of the HeLa cells (cell 1 and cell 2) upon starvation. (C) Three different pathways for the LDs mobilization proposed in the literatures.

during ferroptosis process. All LDs of the two groups have been tracked for more than 60 s (Fig. S35). After analyzing the overall movement trends, we segmented the trajectories of multiple LDs into different types: confined diffusion, directive diffusion, and others (Fig. 5A–B). Here, if the LDs do not exhibit significant changes in intensity during the tracking process but demonstrate jumps in displacement, they are classified as other types. This type of trajectory is likely caused by the jumping between two LDs with the same intensity.

Based on the statistical study of LDs trajectories, it is found that most of the LDs exhibit confined diffusion (93 %) in the control group (Fig. 5C). While after treating with erastin, the LDs displaying confined diffusion are decreased to 71 %. Accordingly, the LDs with directive diffusion are obviously increased from 3 % in control group to 18 % in erastin group. Moreover, the diffusion coefficients of tracking of LDs have been quantified. As shown in Fig. 5D, the treatment with erastin significantly increases the diffusion coefficients for all three types of LDs trajectories. For instance, the average diffusion coefficient for confined diffusion is increased from 5.3×10^{-5} μm²/s to 1.1×10^{-4} μm²/s after erastin treatment, and that value for directive diffusion is boosted from 8.0×10^{-5} μm²/s to 5.2×10^{-4} μm²/s. As a result, the mean diffusion coefficient for all LDs trajectories is largely increased from 5.4×10^{-5} μm²/s to 2.4×10^{-4} μm²/s, which is about a 4.4-fold increase for the erastin treatment (Fig. 5E). Additionally, it is also found that the average movement distance of LDs after erastin stimulation is also obviously larger than that of the control group, being 1.1 μm and 0.40 μm, respectively (Fig. 5F). These imaging results quantitatively indicate that the LDs diffusion is significantly promoted during ferroptosis process. This may be relative to that the lipid peroxidation caused by ferroptosis would stimulate the LDs to move faster and thus supply fresh lipid to various cellular organelles (Olzmann and Carvalho, 2019; Stockwell et al., 2017). To the best of our knowledge, this is the first report to study the 3D-dynamics of LDs at the single LD level.

3.7. Two-photon 3D imaging of tissues

Aside from time-lapse 3D confocal imaging of cells and time-lapse 3D

dynamic tracking of single LD, the fluorescent probe NR-11 has been further successfully applied in two-photon 3D imaging of tissues. As well known, the structure and content of tissues are much more complex than those of cells. Thus, the tissue imaging is very challenging and requires the fluorescent probe with exceptional performance. Here, we have employed the probe NR-11 for two-photon 3D imaging of liver tissues to study the variation of LDs associated with the non-alcoholic fatty liver disease (NAFLD). For this experiment, the liver tissues of control and NAFLD mice have been imaged under the two-photon excitation of 980 nm with precise conditions: a high pixel resolution of 250 nm × 250 nm for xy plane and a small step of 500 nm for z-axis. As shown in Fig. S36A, a total of 220 frames have been continuously recorded in a z-depth of 110 μm for the control mouse liver tissue and then reconstructed to provide a high-quality 3D image. Based on this 3D image, we could clearly visualize the LDs distribution and size in the liver tissue of control mouse. In a similar manner, the 3D image of NAFLD mouse liver tissue has also been captured.

Based on the high-quality two-photon 3D images, we have comprehensively studied the size and density of LDs in normal and NAFLD liver tissues. As for the LDs size distribution (Fig. S36B), it is found that most of the LDs are in a range of 0.3–2 μm for both tissues, while the proportion of large size LDs (above 2 μm) of NAFLD tissue is significantly higher than that of normal tissue. As a result (Fig. S36C–D), the average diameter of LDs of NAFLD tissue and especially the average volume (1.23 ± 0.04 μm, 13.3 ± 1.1 μm³) are obviously larger than those in the normal tissue (0.98 ± 0.02 μm, 3.65 ± 0.47 μm³). Regarding the density of LDs (Fig. S36E), it is interesting to observe that the NAFLD tissue (0.88 ± 0.12 per 1000 μm³) has much a smaller number of LDs in one volume unit than the normal tissue (1.6 ± 0.17 per 1000 μm³). Although the NAFLD tissue has a lower density, its LDs are much larger than those in the normal tissue, the NAFLD tissue (0.65 ± 0.28 %) still displays significantly higher lipid content than normal tissue (0.45 ± 0.05 %) in terms of the volume proportion of LDs in the tissues (Fig. S36F). These imaging results would make a significant contribution to the study of NAFLD.
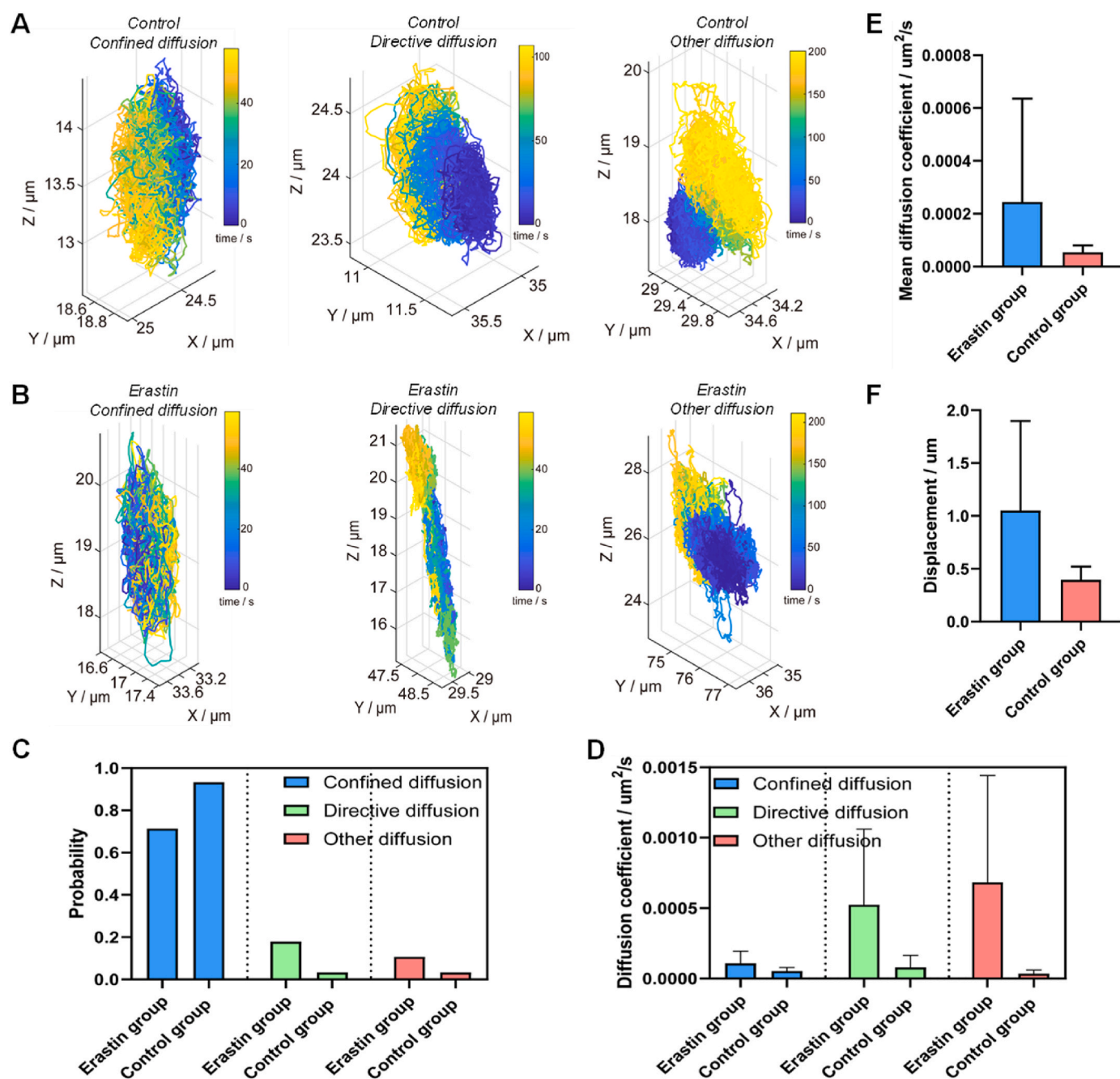
Fig. 5. (A, B) The trajectory of time-lapse 3D dynamic tracking of single LD: different diffusion types of LDs (confined diffusion, directive diffusion, and others) in control group cells and erastin stimulated cells. (C) The statistical study of LDs trajectories in control group cells ($n = 60$) and erastin stimulated cells ($n = 56$). (D) The diffusion coefficients of different diffusion types of LDs in the two cell groups. (E) The mean diffusion coefficients of LDs in the two cell groups. (F) The average movement distances of LDs within 10 s in the two cell groups.

4. Conclusion

In short, we have rationally developed a superior fluorescence probe NR-11 with significantly improved LDs specificity and photostability for advanced fluorescence imaging. It is believed that NR-11 would replace the classical LDs probe Nile Red which has been widely used for 40 years. We will be very happy to freely share this new LDs fluorescence probe with the science community. Moreover, the extensive discussion of the ICT/TICT emission mechanism, the links between molecular structures and properties (LD specificity, photostability), and the new biological insights into LDs would further significantly enhance the importance of this work.

CRediT authorship contribution statement

Huanlong Zheng: Writing – original draft, Investigation. **Hao Sha:** Investigation. **Ri Zhou:** Investigation. **Yu Wu:** Investigation. **Chenguang Wang:** Supervision. **Shangguo Hou:** Supervision. **Geyu Lu:** Supervision.

Declaration of competing interest

The authors declare that they have no known competing financial interests or personal relationships that could have appeared to influence the work reported in this paper.

Acknowledgements

Appendix. ASupplementary data

Supplementary data to this article can be found online at https://doi.org/10.1016/j.bios.2025.117494.

Data availability

Data will be made available on request.

References

Agarwal, N.L., Schaefer, W., 1980. Quinone chemistry. Reaction of 2, 3-dichloro-1, 4-naphthoquinone with 2-aminophenols in pyridine. J. Org. Chem. 45 (25), 5144–5149.

Baral, R.N., Thomas III, S.W., 2015. Steric and electronic substituent effects influencing regioselectivity of tetracene endoperoxidation. J. Org. Chem. 80 (21), 11086–11091.

Bizjak Mali, L., Sepčić, K., Bulog, B., 2013. Long-term starvation in cave salamander effects on liver ultrastructure and energy reserve mobilization. J. Morphol. 274 (8), 887–900.

Cao, M., Liu, Y., Xiang, C., Zheng, G., Xiong, Q., Niu, G., 2025. Versatile organic fluorescent probes for visualizing the dynamics of lipid droplets. Coord. Chem. Rev. 522, 216181.

Chen, J., Qiao, Q., Wang, H., Jiang, W., Liu, W., An, K., Xu, Z., 2024. Clog P-Guided development of multi-colored buffering fluorescent probes for super-resolution imaging of lipid droplet dynamics. Adv. Sci. v2408030.

Chen, J., Wang, C., Liu, W., Qiao, Q., Qi, H., Zhou, W., Xu, N., Li, J., Piao, H., Tan, D., 2021. Stable super-resolution imaging of lipid droplet dynamics through a buffer strategy with a hydrogen-bond sensitive fluorogenic probe. Angew. Chem. Int. Ed. 60 (47), 25104–25113.

Collot, M., Fam, T.K., Ashokkumar, P., Faklaris, O., Galli, T., Danglot, L., Klymchenko, A. S., 2018. Ultrabright and fluorogenic probes for multicolor imaging and tracking of lipid droplets in cells and tissues. J. Am. Chem. Soc. 140 (16), 5401–5411.

Dai, J., Wu, Z., Li, D., Peng, G., Liu, G., Zhou, R., Wang, C., Yan, X., Liu, F., Sun, P., 2023. Super-resolution dynamic tracking of cellular lipid droplets employing with a photostable deep red fluorogenic probe. Biosens. Bioelectron. 229, 115243.

Danylchuk, D.I., Jouard, P.-H., Klymchenko, A.S., 2021. Targeted solvatochromic fluorescent probes for imaging lipid order in organelles under oxidative and mechanical stress. J. Am. Chem. Soc. 143 (2), 912–924.

Gao, W., Cai, L., Kang, F., Shang, L., Zhao, M., Zhang, C., Xu, W., 2023. Bottom-up synthesis of metalated carbyne ribbons via elimination reactions. J. Am. Chem. Soc. 145 (11), 6203–6209.

Greenspan, P., Fowler, S.D., 1985. Spectrofluorometric studies of the lipid probe, nile red. J. Lipid Res. 26 (7), 781–789.

Guo, L., Tian, M., Zhang, Z., Lu, Q., Liu, Z., Niu, G., Yu, X., 2021. Simultaneous two-color visualization of lipid droplets and endoplasmic reticulum and their interplay by single fluorescent probes in lambda mode. J. Am. Chem. Soc. 143 (8), 3169–3179.

Hanaoka, K., Iwaki, S., Yagi, K., Myochin, T., Ikeno, T., Ohno, H., Sasaki, E., Komatsu, T., Ueno, T., Uchigashima, M., 2022. General design strategy to precisely control the emission of fluorophores via a twisted intramolecular charge transfer (TICT) process. J. Am. Chem. Soc. 144 (43), 19778–19790.

Harvald, E.B., Sprenger, R.R., Dall, K.B., Ejsing, C.S., Nielsen, R., Mandrup, S., Murillo, A. B., Larance, M., Gartner, A., Lamond, A.I., 2017. Multi-omics analyses of starvation responses reveal a central role for lipoprotein metabolism in acute starvation survival in C. elegans. Cell Syst. 5 (1), 38–52 e34.

Henwood, A.F., Curtin, N., Estalayo-Adrián, S., Savyasachi, A.J., Gudmundsson, T.A., Lovitt, J.I., Sigurvinsson, L.C., Dalton, H.L., Hawes, C.S., Jacquemin, D., 2024. Time-resolved fluorescence imaging with color-changing. "turn-on/turn-on" AIE nanoparticles. Chem 10 (2), 578–599.

Hong, J., Liu, Y., Tan, X., Feng, G., 2023. Engineering of a NIR fluorescent probe for high-fidelity tracking of lipid droplets in living cells and nonalcoholic fatty liver tissues. Biosens. Bioelectron. 240, 115646.

Hornum, M., Mulberg, M.W., Szomek, M., Reinholdt, P., Brewer, J.R., Wüstner, D., Kongsted, J., Nielsen, P., 2020. Substituted 9-diethylaminobenzo [a] phenoxazin-5-ones (nile red analogues): Synthesis and photophysical properties. J. Org. Chem. 86 (2), 1471–1488.

Hou, S., Exell, J., Welsher, K., 2020. Real-time 3D single molecule tracking. Nat. Commun. 11 (1), 3607.

Kajiwara, K., Osaki, H., Greßies, S., Kuwata, K., Kim, J.H., Gensch, T., Sato, Y., Glorius, F., Yamaguchi, S., Taki, M., 2022. A negative-solvatochromic fluorescent probe for visualizing intracellular distributions of fatty acid metabolites. Nat. Commun. 13 (1), 2533.

Kaur, I., Jia, W., Kopreski, R.P., Selvarasah, S., Dokmeci, M.R., Pramanik, C., McGruer, N. E., Miller, G.P., 2008. Substituent effects in pentacenes: gaining control over HOMO− LUMO gaps and photooxidative resistances. J. Am. Chem. Soc. 130 (48), 16274–16286.

Kong, L., Bai, Q., Li, C., Wang, Q., Wang, Y., Shao, X., Wei, Y., Sun, J., Yu, Z., Yin, J., 2024. Molecular probes for tracking lipid droplet membrane dynamics. Nat. Commun. 15 (1), 9413.

Laval, T., Ouimet, M., 2023. A role for lipophagy in atherosclerosis. Nat. Rev. Cardiol. 20 (7), 431–432.

Liu, G., Zheng, H., Zhou, R., Li, H., Dai, J., Wei, J., Li, D., Meng, X., Wang, C., Lu, G., 2023. Ultrabright organic fluorescent probe for quantifying the dynamics of cytosolic/nuclear lipid droplets. Biosens. Bioelectron. 241, 115707.

Liu, J., Luo, M., Gao, W., Duan, K., Bian, H., Jin, Z., Pan, Y., Wang, S., Gu, Y., Zheng, J., 2025. Dual-responsive two-photon probe for specific lipid droplets near-infrared fluorescence imaging in the brain of epileptic mice. Biosens. Bioelectron. 267, 116774.

Lu, T., Chen, F., 2012. Multiwfn: a multifunctional wavefunction analyzer. J. Comput. Chem. 33 (5), 580–592.

Lu, T., Chen, Q., 2021. Interaction region indicator: a simple real space function clearly revealing both chemical bonds and weak interactions. Chem-Methods 1 (5), 231–239.

Madea, D., Martínek, M., Muchová, L., Vana, J., Vítek, L., Klán, P., 2020. Structural modifications of nile red carbon monoxide fluorescent probe: sensing mechanism and applications. J. Org. Chem. 85 (5), 3473–3489.

Martinez, V., Henary, M., 2016. Nile red and nile blue: applications and syntheses of structural analogues. Chem. Eur. J. 22 (39), 13764–13782.

Mathiowetz, A.J., Olzmann, J.A., 2024. Lipid droplets and cellular lipid flux. Nat. Cell Biol. 26 (3), 331–345.

Nguyen, T.B., Olzmann, J.A., 2017. Lipid droplets and lipotoxicity during autophagy. Autophagy 13 (11), 2002–2003.

Olzmann, J.A., Carvalho, P., 2019. Dynamics and functions of lipid droplets. Nat. Rev. Mol. Cell Biol. 20 (3), 137–155.

Rambold, A.S., Cohen, S., Lippincott-Schwartz, J., 2015. Fatty acid trafficking in starved cells: regulation by lipid droplet lipolysis, autophagy, and mitochondrial fusion dynamics. Dev. Cell 32 (6), 678–692.

Saladin, L., Breton, V., Dal Pra, O., Klymchenko, A.S., Danglot, L., Didier, P., Collot, M., 2023. Dual-color photoconvertible fluorescent probes based on directed photooxidation induced conversion for bioimaging. Angew. Chem. Int. Ed. 62 (4), e202215085.

Shank, N.I., Pham, H.H., Waggoner, A.S., Armitage, B.A., 2013. Twisted cyanines: a non-planar fluorogenic dye with superior photostability and its use in a protein-based fluoromodule. J. Am. Chem. Soc. 135 (1), 242–251.

Shank, N.I., Zanotti, K.J., Lanni, F., Berget, P.B., Armitage, B.A., 2009. Enhanced photostability of genetically encodable fluoromodules based on fluorogenic cyanine dyes and a promiscuous protein partner. J. Am. Chem. Soc. 131 (36), 12960–12969.

Shen, J., Zhou, Y., Yin, L., 2024. Nano/genetically engineered cells for immunotherapy. BMEMat, e12112.

Stockwell, B.R., Angeli, J.P.F., Bayir, H., Bush, A.I., Conrad, M., Dixon, S.J., Fulda, S., Gascón, S., Hatzios, S.K., Kagan, V.E., 2017. Ferroptosis: a regulated cell death nexus linking metabolism, redox biology, and disease. Cell 171 (2), 273–285.

Wan, Y., Chen, W., Liu, Y., Lee, K.W., Gao, Y., Zhang, D., Li, Y., Huang, Z., Luo, J., Lee, C. S., 2024. Neutral cyanine: ultra-stable NIR-II mercocyanines for highly efficient bioimaging and tumor-targeted phototheranostics. Adv. Mater., 2405966

Wang, B., Xi, F., Jin, C., Zhu, H.-L., Tu, M., Li, Z., 2025. A ferrous fluorescence lifetime response probe for monitoring changes in lipid droplets during ferroptosis and imaging in liver disease model. Biosens. Bioelectron. 267, 116742.

Wang, C., Chi, W., Qiao, Q., Tan, D., Xu, Z., Liu, X., 2021a. Twisted intramolecular charge transfer (TICT) and twists beyond TICT: from mechanisms to rational designs of bright and sensitive fluorophores. Chem. Soc. Rev. 50 (22), 12656–12678.

Wang, C., Qiao, Q., Chi, W., Chen, J., Liu, W., Tan, D., McKechnie, S., Lyu, D., Jiang, X.F., Zhou, W., 2020. Quantitative design of bright fluorophores and AIEgens by the accurate prediction of twisted intramolecular charge transfer (TICT). Angew. Chem. Int. Ed. 59 (25), 10160–10172.

Wang, K.N., Liu, L.Y., Mao, D., Xu, S., Tan, C.P., Cao, Q., Mao, Z.W., Liu, B., 2021b. A polarity-sensitive ratiometric fluorescence probe for monitoring changes in lipid droplets and nucleus during ferroptosis. Angew. Chem. Int. Ed. 60 (27), 15095–15100.

Wang, S., Li, X., Chong, S.Y., Wang, X., Chen, H., Chen, C., Ng, L.G., Wang, J.W., Liu, B., 2021c. In vivo three-photon imaging of lipids using ultrabright fluorogens with aggregation-induced emission. Adv. Mater. 33 (11), 2007490.

Wang, W., Chai, L., Chen, X., Li, Z., Feng, L., Hu, W., Li, H., Yang, G., 2023. Imaging changes in the polarity of lipid droplets during NAFLD-induced ferroptosis via a red-emitting fluorescent probe with a large stokes shift. Biosens. Bioelectron. 231, 115289.

Wang, Y., Song, Y., Xu, L., Zhou, W., Wang, W., Jin, Q., Xie, Y., Zhang, J., Liu, J., Wu, W., 2024. A membrane-targeting aggregation-induced emission probe for monitoring lipid droplet dynamics in Ischemia/reperfusion-induced cardiomyocyte ferroptosis. Adv. Sci., 2309907

Wu, S., Li, X., Zhou, M., Cui, Y., Wu, W., Ping, J., Guo, X., Hu, Q., 2024. pH-triggered hydrophility-adjustable fluorescent probes for simultaneously imaging lipid droplets and lysosomes and the application in fatty liver detection. Biosens. Bioelectron. 251, 116084.

Xiong, T., Chen, Y., Peng, Q., Lu, S., Long, S., Li, M., Wang, H., Lu, S., Chen, X., Fan, J., 2024. Lipid droplet targeting type I photosensitizer for ferroptosis via lipid peroxidation accumulation. Adv. Mater. 36 (4), 2309711.

Zadoorian, A., Du, X., Yang, H., 2023. Lipid droplet biogenesis and functions in health and disease. Nat. Rev. Endocrinol. 19 (8), 443–459.

Zhang, W., Kong, J., Miao, R., Song, H., Ma, Y., Zhou, M., Fang, Y., 2024. Integrating aggregation induced emission and twisted intramolecular charge transfer via molecular engineering. Adv. Funct. Mater. 34 (7), 2311404.